


# Self-regeneration of supported transition metals by a high entropy-driven principle

Shengtai Hou<sup>1</sup>, Xuefeng Ma<sup>1</sup>, Yuan Shu<sup>1</sup>, Jiafeng Bao<sup>1</sup>, Qiuyue Zhang<sup>2</sup>, Mingshu Chen<sup>2</sup>, Pengfei Zhang<sup>1</sup>  <sup>✉</sup> & Sheng Dai<sup>3</sup>

The sintering of Supported Transition Metal Catalysts (STMCs) is a core issue during high temperature catalysis. Perovskite oxides as host matrix for STMCs are proven to be sintering-resistance, leading to a family of self-regenerative materials. However, none other design principles for self-regenerative catalysts were put forward since 2002, which cannot satisfy diverse catalytic processes. Herein, inspired by the principle of high entropy-stabilized structure, a concept whether entropy driving force could promote the self-regeneration process is proposed. To verify it, a high entropy cubic  $Zr_{0.5}(NiFeCuMnCo)_{0.5}O_x$  is constructed as a host model, and interestingly in situ reversible exsolution-dissolution of supported metallic species are observed in multi redox cycles. Notably, in situ exsolved transition metals from high entropy  $Zr_{0.5}(NiFeCuMnCo)_{0.5}O_x$  support, whose entropic contribution ( $T\Delta S_{con}^{reg} = T\star 12.7 \text{ J mol}^{-1} \text{ K}^{-1}$ ) is predominant in  $\Delta G$ , affording ultrahigh thermal stability in long-term  $\text{CO}_2$  hydrogenation (400 °C, >500 h). Current theory may inspire more STWCs with excellent sintering-resistance performance.

<sup>1</sup>School of Chemistry and Chemical Engineering, Shanghai Jiao Tong University, Shanghai 200240, China. <sup>2</sup>State Key Laboratory of Physical Chemistry of Solid Surfaces, National Engineering Laboratory for Green Chemical Productions of Alcohols-Ethers-Esters, Department of Chemistry, College of Chemistry and Chemical Engineering, Xiamen University, Xiamen 361005, China. <sup>3</sup>Chemical Sciences Division, Oak Ridge National Laboratory, Oak Ridge, TN 37831, USA. ✉email: [chemistryzpf@sjtu.edu.cn](mailto:chemistryzpf@sjtu.edu.cn)

Supported metal catalysts are of great importance in both industrial and fundamental catalysis<sup>1</sup>. The methods for generating active sites on metal oxide carriers include chemical or physical deposition techniques (e.g., impregnation method<sup>2</sup>, deposition-precipitation method<sup>3</sup>, co-precipitation process<sup>4</sup>, atomic layer deposition<sup>5</sup>, spraying<sup>6</sup> and so on<sup>7</sup>). Needless to say, those methods have significantly promoted the synthetic chemistry of supported metal catalysts. For example, the control of metal nanocrystal size by modified deposition method reveals the attractive role of corner atoms, which offers a theoretical guidance for catalyst design<sup>8</sup>. Nevertheless, the deactivation of supported metal catalysts, especially those metal nanoparticles (NPs) with low tamman temperatures (e.g., Cu<sup>9</sup>, Ag<sup>10</sup>, Au<sup>11</sup>) and high surface energies<sup>12</sup>, is often inevitable by sintering<sup>13</sup> under long-term exposure to the high temperature or redox environments. For example, Au/TiO<sub>2</sub> catalysts afforded an ultralow temperature for CO oxidation<sup>14</sup>, while particle growth leading to the activity loss often occurred during high temperature operation<sup>15</sup>.

Early in this century, a self-regenerative strategy by in situ exsolution of active species from host matrix was presented by Nishihata's group<sup>16</sup>, which can greatly prolong the lifetime of three-way catalysts. The emergence of perovskite-based (ABO<sub>3</sub>) self-regenerative catalysts exploits a useful approach to optimize catalyst activity and stability<sup>16–21</sup>. To our knowledge, the control of nonstoichiometry<sup>18</sup> (A-site defect interactions), judicious choice of B-site composition (e.g., Pd<sup>17</sup>, Pt<sup>22</sup>, Ni<sup>23</sup>, CoFe alloy<sup>24</sup>) and the surface modification (polished or pre-treated perovskite) are frequently used to tailor B-site metals exsolution. This type of catalytic materials can not only in situ generate active sites, but also accomplish reintegration of those species back to parent perovskites during oxidation-reduction cycles<sup>16–21</sup>. Meanwhile, introducing high-valence cations (Nb<sup>25</sup>, Ti<sup>26</sup>, Ga<sup>27</sup>, etc.) into ABO<sub>3</sub> structure can improve the structural stability of the parent perovskites, which contributes to the reintegration process during catalysis<sup>19</sup>. This process effectively suppresses the sintering or agglomeration of the supported metals<sup>16</sup>. However, these types of host matrix are limited to perovskite crystal structures and the state-of-art self-generation systems are perovskite-based catalysts<sup>16–19</sup> (Fig. 1a), which cannot meet the broad requirements by different catalytic processes. To date, the proposal of a self-regenerative principle for the design of sintering-resistance catalysts is still desired.

Since the discovery of high entropy alloys in 2004<sup>28</sup> and the pioneering introduction of high-entropy oxides (HEOs: oxide solid solutions contain five or more distinct metal cations) in 2015<sup>29</sup>, entropy-stabilized materials such as oxides<sup>30</sup>, sulfides<sup>31</sup>, phosphide<sup>32</sup>, nitrides<sup>33</sup>, carbides<sup>34</sup>, and borides<sup>35</sup>, are flourishing in the library of advanced materials during past five years. Inspired by the principle of thermodynamics<sup>29,30</sup> (Entropic contribution could predominate the thermodynamic landscape), applying the theory of high entropy materials to trigger the self-regeneration during catalytic redox processes may be a choice. First, based on the configurational entropy<sup>34</sup> (it refers to the number of conformations of a molecule and the number of ways that atoms or molecules pack together in the oxide) formula (Fig. 1.b), more disorder of system and higher randomness of structure with a lower Gibbs free energy can contribute to the stability of host structure, especially during high temperature catalysis ( $\Delta G = H - T\Delta S$ )<sup>31,36</sup> (Fig. 1.bii). From another perspective, the reintegration process can be promoted due to an entropy-added motivation by the oxidative transformation of isolated metals back into parent metal oxides. The theoretical conjecture stimulates us to carry out a number of representative experiments.

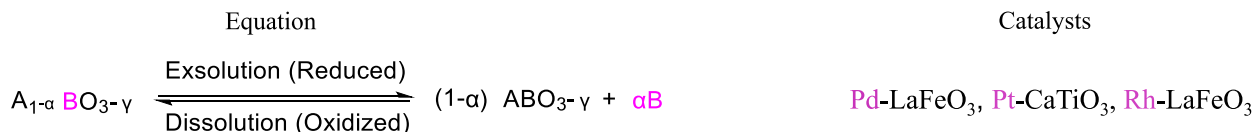
In this work, we verify the entropy-driven principle for self-regenerative catalyst by high entropy ZrO<sub>2</sub>. A single-phase cubic Zr<sub>0.5</sub>(NiFeCuMnCo)<sub>0.5</sub>O<sub>x</sub>, whose entropic contribution ( $T\Delta S_{config} = T \cdot 12.7 \text{ J mol}^{-1} \text{ K}^{-1}$ ) is predominant in  $\Delta G$ <sup>28,29,31</sup>, was prepared and rationally selected as a model catalyst. Interestingly, reductive H<sub>2</sub> treatment could induce the exsolution of CoFeCuNi alloy NPs on the surface of parent high entropy ZrO<sub>2</sub> NPs. With high entropy Zr<sub>0.5</sub>(NiFeCuMnCo)<sub>0.5</sub>O<sub>x</sub> as the host matrix, the exsolution and reintegration of CoFeCuNi alloy were observed during three redox cycles (H<sub>2</sub> 600 °C + Air 550 °C), an interesting feature that may confine metal species under dynamics catalysis (Fig. 1.biii). As a proof of principle, the entropy-driven self-regenerative property endows Zr<sub>0.5</sub>(NiFeCuMnCo)<sub>0.5</sub>O<sub>x</sub> catalyst good stability during CO<sub>2</sub> hydrogenation reaction. The Zr<sub>0.5</sub>(NiFeCuMnCo)<sub>0.5</sub>O<sub>x</sub> catalyst functioned well at 400 °C during 500 h continuous hydrogenation, and at the same time no phase separation or sintering were found on the reused catalyst. The self-regenerative talent of high entropy material may open an alternative for the design of sintering-resistance catalysts.

## Results

**The formation of high entropy cubic Zr<sub>0.5</sub>(NiFeCuMnCo)<sub>0.5</sub>O<sub>x</sub>.** Inspired by the principle of the high entropy-stabilized structure, the synthesis of high entropy ZrO<sub>2</sub> catalyst was carefully investigated by a mechanochemical process (Fig. 2). Five common transition metal salts (Ni, Fe, Cu, Mn, Co) were mixed with ZrCl<sub>4</sub> and NaOH, followed by calcination in air and sodium salt removal. Definitely, for transition metal dopants, the matching radius (the rationally selected five metals  $|\frac{r_{Zr} - r_x}{r_{Zr}}| < 20\%$ <sup>37</sup>: Ni, Fe, Cu, Mn, Co) was a crucial factor for achieving the highly doped ZrO<sub>2</sub> solid solution. Binary doped ZrO<sub>2</sub> samples were initially prepared. Impure phases were found (Supplementary Fig. 1) in Zr<sub>0.5</sub>Cu<sub>0.5</sub>O<sub>x</sub>, Zr<sub>0.5</sub>Mn<sub>0.5</sub>O<sub>x</sub>, Zr<sub>0.5</sub>Co<sub>0.5</sub>O<sub>x</sub>, and Zr<sub>0.5</sub>Ni<sub>0.5</sub>O<sub>x</sub>, presumably due to the limited solubility of the dopants in ZrO<sub>2</sub><sup>38</sup>. At current stage, it is still difficult to incorporate 50 mol% dopants into monocryalline ZrO<sub>2</sub><sup>39</sup>. In addition, a series of Zr<sub>0.9</sub>M<sub>0.1</sub>O<sub>x</sub> (M: Co, Ni, Mn, Cu, Fe) materials were constructed by the same synthesis conditions. Meanwhile, the doped metal content is the same as Zr<sub>0.5</sub>Ni<sub>0.1</sub>Fe<sub>0.1</sub>Cu<sub>0.1</sub>Mn<sub>0.1</sub>Co<sub>0.1</sub>O<sub>x</sub> sample. Deserved to be mentioned, the Zr<sub>0.9</sub>Cu<sub>0.1</sub>O<sub>x</sub>, Zr<sub>0.9</sub>Ni<sub>0.1</sub>O<sub>x</sub> exhibited obvious impurity peaks, which could be ascribed to the CuO, NiO, respectively (Supplementary Fig. 2a, b). It seems reasonable that 10% Cu-doped and 10% Ni-doped ZrO<sub>x</sub> materials would present obvious diffraction peaks of NiO and CuO. The enhancement of entropic contribution may compensate the formation enthalpy<sup>40</sup>, and then a detailed study for constructing high entropy Zr<sub>0.5</sub>(NiFeCuMnCo)<sub>0.5</sub>O<sub>x</sub> was carried out.

Firstly, the calcination temperature was adjusted to explore the phase evolution of Zr<sub>0.5</sub>(NiFeCuMnCo)<sub>0.5</sub>O<sub>x</sub> precursors. As shown in the Fig. 3a, obvious diffraction peaks for the typical cubic ZrO<sub>2</sub> phase started to form at 550 °C. Notably, no other impurity peaks were observed at an elevated temperature (e.g., 600 °C). This phenomenon indicated the possible formation of a high entropy cubic Zr<sub>0.5</sub>(NiFeCuMnCo)<sub>0.5</sub>O<sub>x</sub>. Then, the solubility of five metals (Ni, Fe, Cu, Mn, Co) within ZrO<sub>2</sub> solid solution was carefully investigated by adjusting their total ratio (0.3–0.9) (Fig. 3b). The single cubic structure of ZrO<sub>2</sub> was well maintained in Zr<sub>0.7</sub>(NiFeCuMnCo)<sub>0.3</sub>O<sub>x</sub> and Zr<sub>0.5</sub>(NiFeCuMnCo)<sub>0.5</sub>O<sub>x</sub>, while impure reflections of other crystal structures were detected with a higher ratio (0.7–0.9) of doped metals (Fig. 3b). The molar ratio (Zr:Ni:Fe:Cu:Mn:Co = 5:1:1:1:1) was then fixed, and a relative high configurational entropy ( $S_{config} = 12.47 \text{ J mol}^{-1} \text{ K}^{-1}$ ) could be expected.

a. Traditional Perovskite-based Systems



b. This Work: High Entropy Zirconia

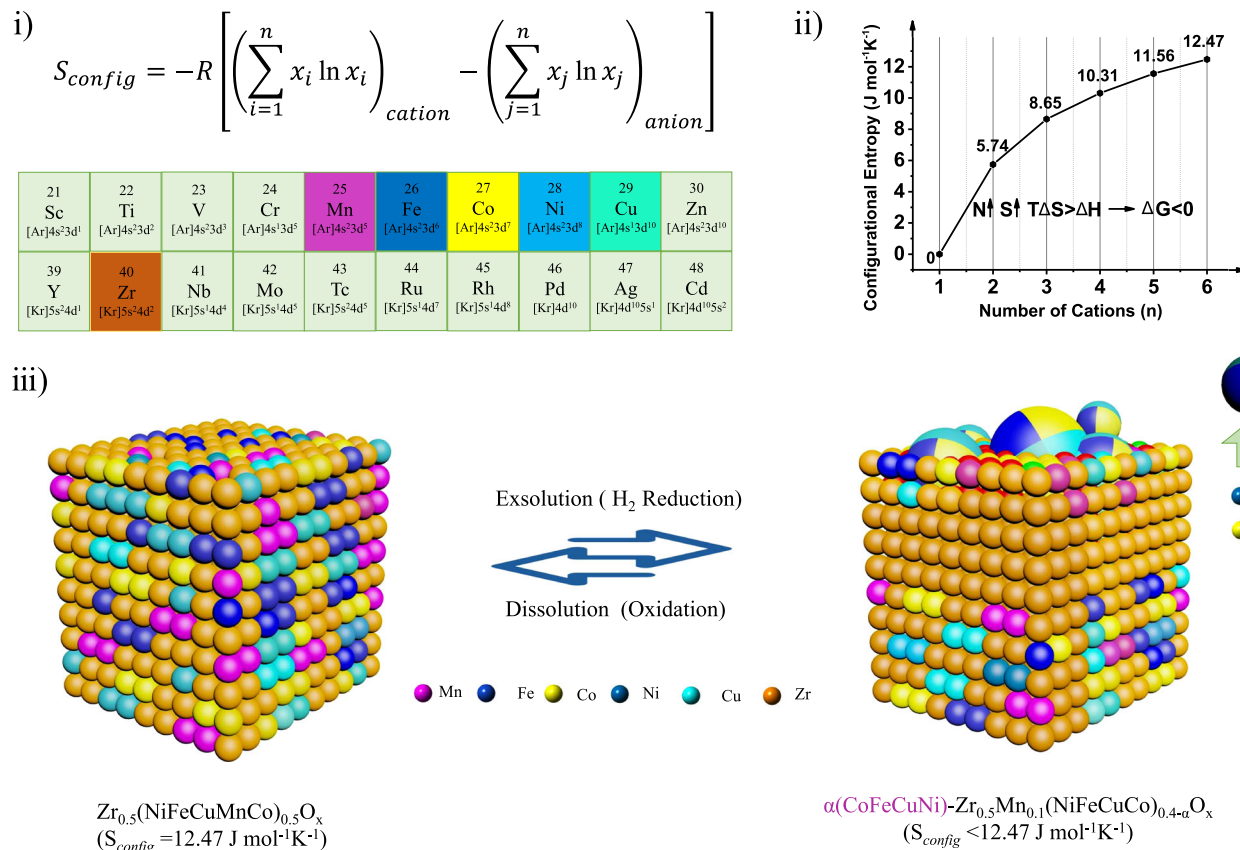


**Fig. 1 Comparison of self-regenerative materials.** **a** Representative perovskite-based self-regenerative materials. **b** i. The configurational entropy formula, and the selected metals for high entropy ZrO<sub>2</sub>. ii. Calculated values of configurational entropy for Zr<sub>0.5</sub>(M<sub>1</sub>-M<sub>n</sub>)<sub>0.5</sub>O<sub>x</sub>, n = 1-5 (for example, n = 2, Zr<sub>0.5</sub>(M<sub>1</sub>M<sub>2</sub>)<sub>0.5</sub>O<sub>x</sub>). iii. Schematic representation of in situ exsolution and dissolution of CoFeCuNi alloys in the Zr<sub>0.5</sub>(NiFeCuMnCo)<sub>0.5</sub>O<sub>x</sub> during redox processes. For simple, oxygen ions were omitted.

Rietveld refinement was then performed to determine the structural parameters of Zr<sub>0.5</sub>(NiFeCuMnCo)<sub>0.5</sub>O<sub>x</sub>. The initial structural model was built based on the cubic ZrO<sub>2</sub> (a = b = c = 5.100 Å). The calculated lattice constant of Zr<sub>0.5</sub>(NiFeCuMnCo)<sub>0.5</sub>O<sub>x</sub> was a = b = c = 5.097 Å (Fig. 3c, d). The difference in atomic sizes between Zr and transition metals would cause the shrinkage of the lattice of ZrO<sub>2</sub> matrix<sup>41</sup>. However, it should be noted that the abundance of oxygen vacancies in doped ZrO<sub>2</sub> may enlarge the ZrO<sub>2</sub> lattice<sup>42</sup>. Meanwhile, the R-factor (Rp (%))=4.6), weighted profiles R-factor (Rwp (%))=4.7) and chi square (χ<sup>2</sup> = 1.330) of the HE ZrO<sub>2</sub> were quite good (Fig. 3c). The simulated PXRD pattern of the high entropy ZrO<sub>2</sub> was in good agreement with the experimental one. Those XRD results suggest the formation of cubic Zr<sub>0.5</sub>(NiFeCuMnCo)<sub>0.5</sub>O<sub>x</sub>.

With the option temperature (550 °C) and composition in hand, a high specific surface area (84 m<sup>2</sup> g<sup>-1</sup>) was obtained by

optimizing the dosage of NaCl additive (Supplementary Table 1. Supplementary Fig. 3). To the best of our knowledge, the high temperature for phase transformation (e.g., 900–1300 °C) in entropy-driving force (TΔS) would cause the collapse of pores, leading to HEOs with low surface areas, such as, NiMgCuZnCoOx by solid-state combustion (2 m<sup>2</sup> g<sup>-1</sup>)<sup>43</sup>, NiMgCuZnCoOx by citric acid-based sol-gel method (28 m<sup>2</sup> g<sup>-1</sup>)<sup>43</sup>, (MgTiZnCu-Fe)<sub>3</sub>O<sub>4</sub> by solid-state combustion (12 m<sup>2</sup> g<sup>-1</sup>)<sup>44</sup>, CoNiCuMgZnOx with graphene oxide as a sacrificial template (42 m<sup>2</sup> g<sup>-1</sup>)<sup>45</sup>. The current porosity (84 m<sup>2</sup> g<sup>-1</sup>) may be attributed to the particle breakage by mechanochemistry<sup>46</sup>, and meanwhile a mild crystallization temperature (550 °C) could effectively avoid the excessive growth of fine NPs and interstitial porosity was retained<sup>47</sup>.

In order to observe the morphology of the Zr<sub>0.5</sub>(NiFeCuMnCo)<sub>0.5</sub>O<sub>x</sub> sample, the high-angle annular dark-field signal (HAADF) and energy dispersive spectrometer (EDS) elemental

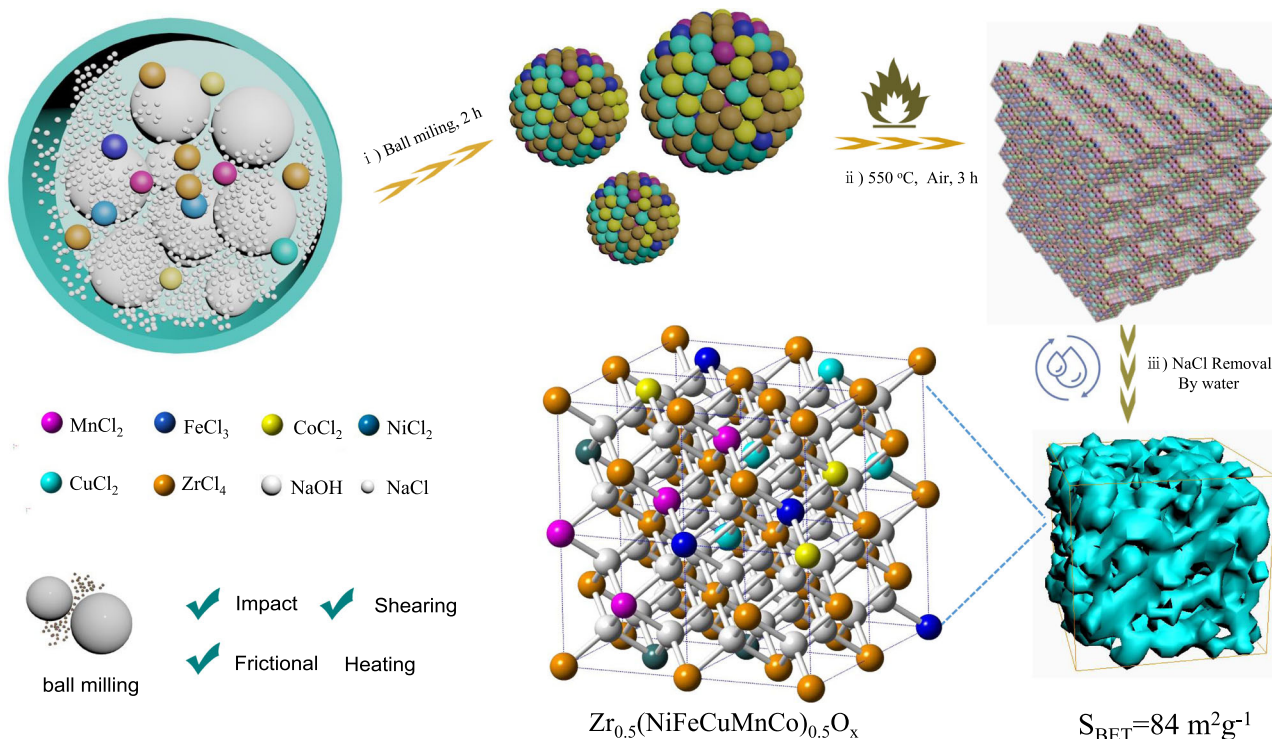


**Fig. 2** The synthetic route of entropy-stabilized  $Zr_{0.5}(NiFeCuMnCo)_{0.5}O_x$ . i Mixing metal chlorates  $ZrCl_4$ ,  $MnCl_2$ ,  $NiCl_2$ ,  $FeCl_3$ ,  $CoCl_2$ ,  $CuCl_2$ ,  $NaCl$  and  $NaOH$  by ball milling. ii Calcination of the intermediate in air. iii Sodium salt removal from the composite by washing.

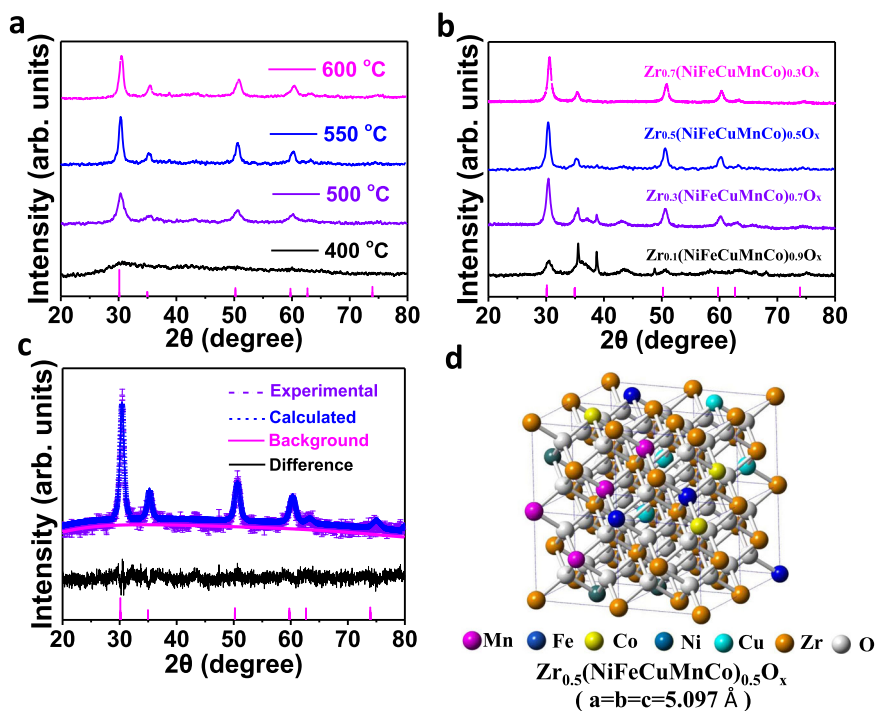


**Fig. 3** The synthesis of a cubic phase  $Zr_{0.5}(NiFeCuMnCo)_{0.5}O_x$ . **a** The phase evolution of  $Zr_{0.5}(NiFeCuMnCo)_{0.5}O_x$  precursors under different calcination temperatures. **b** The P-XRD patterns of  $ZrO_2$  doped with different total ratio (0.3–0.9) of five metals. **c** P-XRD patterns together with Rietveld fits of the  $Zr_{0.5}(NiFeCuMnCo)_{0.5}O_x$  sample prepared at 550 °C. **d** Structural view of cubic  $Zr_{0.5}(NiFeCuMnCo)_{0.5}O_x$ . arb. units: arbitrary unit.

maps were performed (Fig. 4).  $Zr_{0.5}(NiFeCuMnCo)_{0.5}O_x$  was composed of small NPs (e.g., 10–30 nm), which aggregated together and resulted in abundant interstitial porosity. This feature was in agreement with the found  $N_2$  sorption isotherm of

$Zr_{0.5}(NiFeCuMnCo)_{0.5}O_x$  ( $S_{BET} = 84 \text{ m}^2 \text{ g}^{-1}$ ). Moreover, the EDS elemental maps of individual metals showed that the five dopants were homogeneously distributed in the  $ZrO_2$  backbone, suggesting that five metals-doped  $ZrO_2$  solid solution was constructed.



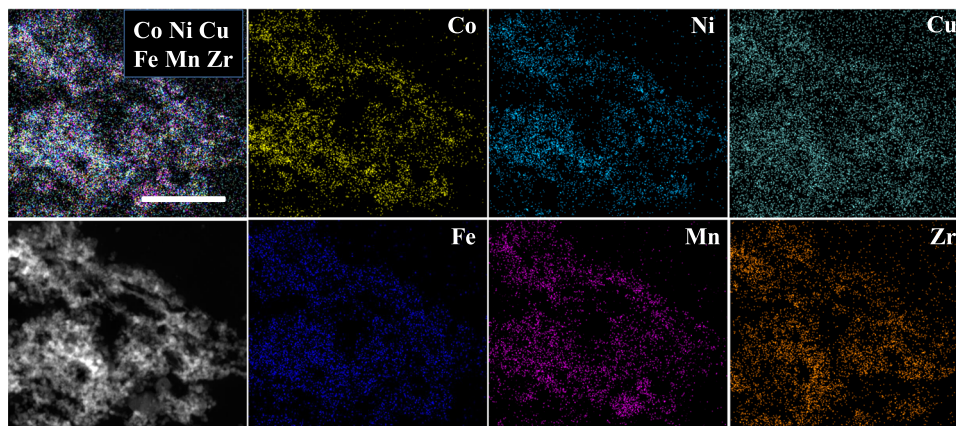


**Fig. 4** The characterization of freshly made  $\text{Zr}_{0.5}(\text{NiFeCuMnCo})_{0.5}\text{O}_x$ . STEM-HAADF image and EDS elemental maps of  $\text{Zr}_{0.5}(\text{NiFeCuMnCo})_{0.5}\text{O}_x$ . Scale bar, 200 nm.

Meanwhile, the molar ratio of elements (Zr:Ni:Fe:Cu:Mn:Co) in  $\text{Zr}_{0.5}(\text{NiFeCuMnCo})_{0.5}\text{O}_x$  material was confirmed to be 5.7:1:1.1:1:1.1:1.1 by inductively coupled plasma mass spectrometer (Supplementary Table 2), which matched well with the theoretical formula. These investigations encouraged us to explore its self-regeneration possibility during redox cycles.

**The exploration of self-regeneration process.** To verify the exsolution and reintegration behavior, several exploratory experiments were carried out with high entropy  $\text{Zr}_{0.5}(\text{NiFeCuMnCo})_{0.5}\text{O}_x$  as a model. The exsolution of metals was determined by the reducibility of transition metal oxides<sup>48</sup>, and it was closely related to co-segregation energy (transition metal accompanying with oxygen vacancies)<sup>49</sup>. The  $\text{ZrO}_2$  doped with low valence metals could contribute to produce oxygen vacancies<sup>50</sup>, which promoted the exsolution of metals<sup>51</sup> under reductive atmosphere. Subsequently, the  $\text{H}_2$ -TPR spectrum was tested to probe the reduction behavior of  $\text{Zr}_{0.5}\text{Co}_{0.5}\text{O}_x$ ,  $\text{Zr}_{0.5}\text{Ni}_{0.5}\text{O}_x$ ,  $\text{Zr}_{0.5}\text{Cu}_{0.5}\text{O}_x$ ,  $\text{Zr}_{0.5}\text{Fe}_{0.5}\text{O}_x$ ,  $\text{Zr}_{0.5}\text{Mn}_{0.5}\text{O}_x$ ,  $\text{Zr}_{0.5}\text{Mn}_{0.25}\text{Cu}_{0.25}\text{O}_x$  (Supplementary Fig. 4) and pristine  $\text{Zr}_{0.5}(\text{NiFeCuMnCo})_{0.5}\text{O}_x$  samples (Supplementary Fig. 5). As shown in Supplementary Fig. 4a, the peak at 256 °C resulted from the reduction of  $\text{CuO}$  to  $\text{Cu}$ <sup>52</sup>. For  $\text{Zr}_{0.5}\text{Mn}_{0.5}\text{O}_x$  sample (Supplementary Fig. 4b), the two reduction peaks were considered as  $\text{MnO}_2$  or  $\text{Mn}_2\text{O}_3$  to  $\text{Mn}_3\text{O}_4$  (318 °C), and  $\text{Mn}_3\text{O}_4$  to  $\text{MnO}$  (420 °C)<sup>53</sup>. For  $\text{Zr}_{0.5}\text{Mn}_{0.25}\text{Cu}_{0.25}\text{O}_x$  sample (Supplementary Fig. 4c), the reduction peaks at 269 °C and 325 °C were attributed to the reduction of the  $\text{CuO}$  to  $\text{Cu}^0$  and manganese oxides to  $\text{MnO}$ , respectively<sup>54</sup>. All three types of nickel oxide (363, 467, 570 °C) were reduced to the  $\text{Ni}^0$  (Supplementary Fig. 4d)<sup>55</sup>. For  $\text{Zr}_{0.5}\text{Fe}_{0.5}\text{O}_x$  sample (Supplementary Fig. 4e), the TPR profile showed two distinct reduction peaks. The peak centered at 401 °C was assigned to the reduction of  $\text{Fe}_2\text{O}_3$  to  $\text{Fe}_3\text{O}_4$  and the peak at 566 °C was ascribed to the reduction of  $\text{Fe}_3\text{O}_4$  to  $\text{Fe}^0$ <sup>56</sup>. For cobalt-doped sample (Supplementary Fig. 4f), the reduction peaks around 295 °C and 408 °C were attributed to the transitions from  $\text{Co}^{3+}$  to  $\text{Co}^{2+}$  and  $\text{Co}^{2+}$  to  $\text{Co}^0$ <sup>57</sup>. Indeed, the addition of  $\text{CuO}$  could decrease the reduction temperature (Supplementary Fig. 4a, b, c)<sup>54</sup>. Interestingly, only one strong reduction peak was observed at ~279 °C for  $\text{Zr}_{0.5}(\text{NiFeCuMnCo})_{0.5}\text{O}_x$  sample (Supplementary Fig. 5). Then, with  $\text{CuO}$  as the standard reference, the  $\text{H}_2$  consumption of  $\text{Zr}_{0.5}(\text{NiFeCuMnCo})_{0.5}\text{O}_{1.1+y}$  sample (1.1 ascribes to unreducible  $\text{ZrO}_2$ <sup>58</sup>, and  $\text{MnO}$ <sup>49</sup>) can reach 3.63  $\text{mmol g}^{-1}$ . Then, the  $y$  value is calculated to be 0.36<sup>59</sup>. In addition, the  $y$  values of other samples were provided (Supplementary Table 3). Based on this result, the  $\text{Zr}_{0.5}(\text{NiFeCuMnCo})_{0.5}\text{O}_{1.46}$  formula suggests that significant

amount of oxygen vacancies were created. Hence, these preliminary studies encourage further research about the exsolution process.

Subsequently, the pristine high entropy  $\text{Zr}_{0.5}(\text{NiFeCuMnCo})_{0.5}\text{O}_x$  was treated in reduction condition ( $\text{H}_2$ ) at appointed temperatures for 2 h. As shown in Fig. 5a, the early stage of phase transformation was not clear at 400 °C. When the reduction temperature raised to 500–600 °C, the diffraction pattern of the exsolution phase showed a broad peak at 44 °C, which could be assigned to the reflection of transition metals (111). At the same time, typical peaks for cubic  $\text{ZrO}_2$  were still preserved during  $\text{H}_2$  treatment. In sharp contrast, the exsolution diffraction peaks of as-prepared binary  $\text{Zr}_{0.5}\text{Cu}_{0.5}\text{O}_x$  were sharp, revealing the excessive growth of  $\text{Cu}$  particles (average particle size by Reitveld refinement analysis: 37.7 nm)<sup>60</sup> (Fig. 5b, Supplementary Fig. 6). Meanwhile, the exsolution peaks of quaternary  $\text{Zr}_{0.5}(\text{NiCuCo})_{0.5}\text{O}_x$  presented two different phases (Fig. 5b). The multi redox behavior of  $\text{Zr}_{0.5}(\text{NiFeCuMnCo})_{0.5}\text{O}_x$  was detailedly studied in the following (Fig. 5c). Therefore, high-entropy  $\text{Zr}_{0.5}(\text{NiFeCuMnCo})_{0.5}\text{O}_x$  as a host matrix could somewhat suppress the growth or agglomeration of exsolved metal NPs even under harsh reductive conditions (e.g., 600 °C), which stood on the surface of parent high entropy  $\text{ZrO}_2$  NPs.

Then, the  $\text{Zr}_{0.5}(\text{NiFeCuMnCo})_{0.5}\text{O}_x$  (treated at 400 °C,  $\text{H}_2$ ) was investigated by STEM and elemental mapping analysis. Firstly, STEM was employed to provide insights into the exsolved NPs in  $\text{Zr}_{0.5}(\text{NiFeCuMnCo})_{0.5}\text{O}_x$  under reducing atmosphere. As shown in Supplementary Fig. 7, reductive  $\text{H}_2$  treatment induced the exsolution of grains growing on the surface of parent high entropy  $\text{ZrO}_2$  NPs. Meanwhile, elemental mapping analysis exhibited aggregation of some elements (Supplementary Fig. 7b). To further confirm the exsolved metal species, the high resolution elemental mapping images at the edge of the sample revealed the formation of the  $\text{CoFeCuNi}$  alloy NPs (Fig. 6). To further study clearly the metal exsolution, the O elemental mapping was added (Supplementary Fig. 8). A typical particle on the edge was highlighted by yellow circle. It showed a relatively low O content, close to the background. This result somewhat demonstrated the formation of the metallic  $\text{CoFeCuNi}$  particle.

To further understand current observation, in situ high-resolution XPS (Fig. 7a, b) was carried out to investigate the surface state of the  $\text{Zr}_{0.5}(\text{NiFeCuMnCo})_{0.5}\text{O}_x$  during  $\text{H}_2$  treatment from RT to 873 K. As shown in Fig. 7c, the peak centered at 778.3 eV was assigned to the characteristic  $\text{Co } 2P_{3/2}$  peak of  $\text{Co}^0$ <sup>61</sup>. Meanwhile, the sharp peak at 852.7 eV resulted from surface  $\text{Ni}^0$  (Fig. 7d)<sup>61</sup>. Since the Binding Energy of  $\text{Cu}^+$  generally overlaps with  $\text{Cu}^0$  in the  $\text{Cu } 2P$  core level (Fig. 7e, peak

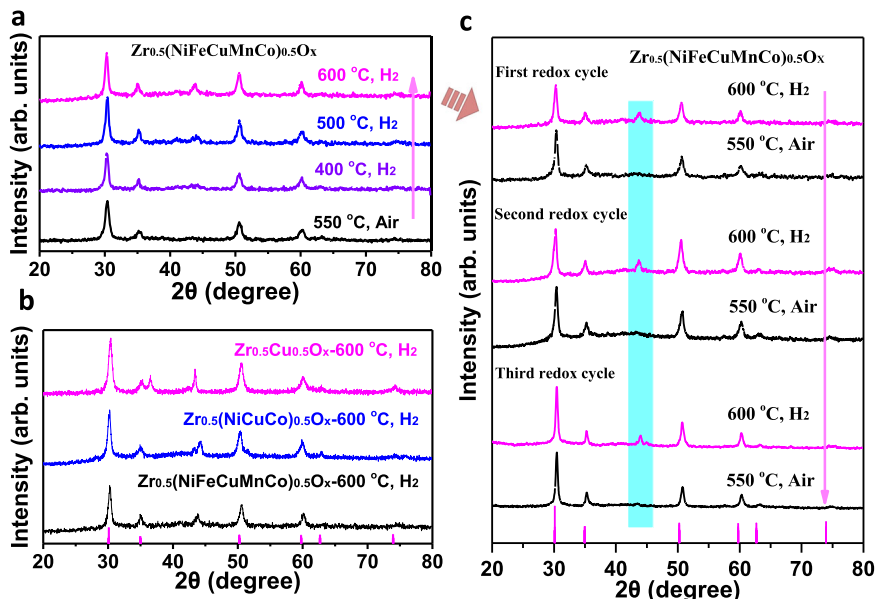


**Fig. 5** The XRD patterns of doped  $ZrO_x$  samples during redox processes. **a** The P-XRD patterns of  $Zr_{0.5}(\text{NiFeCuMnCo})_{0.5}O_x$  treated at 10%  $H_2$  balance with  $N_2$  at appoint temperature (400, 500, 600 °C) for 2 h. **b** The P-XRD patterns of  $Zr_{0.5}Cu_{0.5}O_x$ ,  $Zr_{0.5}(\text{NiCuCo})_{0.5}O_x$ , and  $Zr_{0.5}(\text{NiFeCuMnCo})_{0.5}O_x$  treated at 10%  $H_2$  balance with  $N_2$  at 600 °C for 2 h. **c** the P-XRD patterns of phase evolution in multi cycles between reductive and oxidative conditions. arb. units: arbitrary unit.

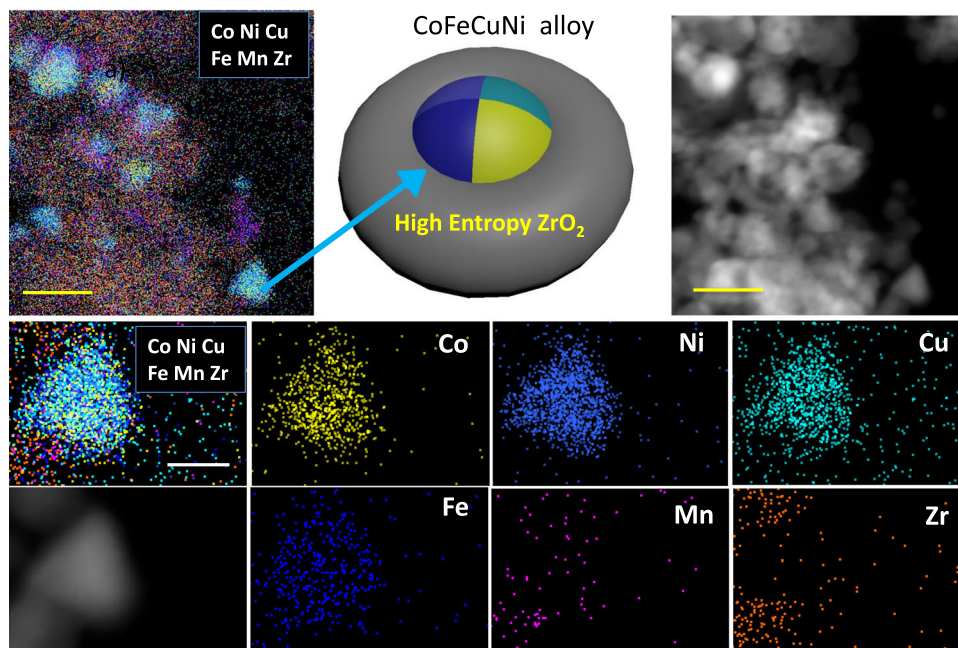


**Fig. 6** The characterization of  $H_2$ -reduced  $Zr_{0.5}(\text{NiFeCuMnCo})_{0.5}O_x$ . STEM-HAADF images and EDS elemental maps of  $Zr_{0.5}(\text{NiFeCuMnCo})_{0.5}O_x$  (treated at 400 °C,  $H_2$ ). Yellow scale bar, 30 nm. White scale bar, 10 nm.

at 932.6 eV), the X-ray induced Auger electron spectra in the kinetic energy region of 928–906 eV is provided in Fig. 7f. As shown in Fig. 7f, the kinetic energy at 918.6 eV could be contributed to  $Cu^0$ <sup>61</sup>. A signal peak is located at 706.9 eV, which is ascribed to the Fe  $2P_{3/2}$  metal (Fig. 7g)<sup>61</sup>. As expected, there is no peak for  $Mn^0$  at 638.8 eV<sup>61</sup>. Meanwhile,  $MnO$   $2P_{3/2}$  (at 641.0 eV) peaks show their characteristic satellite peak at 636.9 eV (Fig. 7h)<sup>62</sup>. Indeed, manganic oxide is more difficult to be reduced to  $Mn^0$ <sup>63</sup>. Under  $H_2$  treatment, several transition metal ions (Co, Ni, Cu, Fe) seem to in situ migrate and separate from the bulk of high entropy

$Zr_{0.5}(\text{NiFeCuMnCo})_{0.5}O_x$ , while the original cubic  $ZrO_2$  matrix was well maintained (Fig. 5a). The  $H_2$ -induced formation of exsolved CoNiCuFe NPs is different with the Cantor alloy (FeCrMnNiCo) by melting process<sup>64</sup> and those CoNiCuFe NPs could not be described as high entropy alloys<sup>65</sup>. As illustrated in Supplementary Fig. 5, only one strong reduction peak was observed at  $\sim 279$  °C, which could be assigned to the produce of the CoFeCuNi alloy. Based on these results, the exsolution phenomenon of alloys occurred under reductive atmosphere, which was just the first step of self-regenerative process.

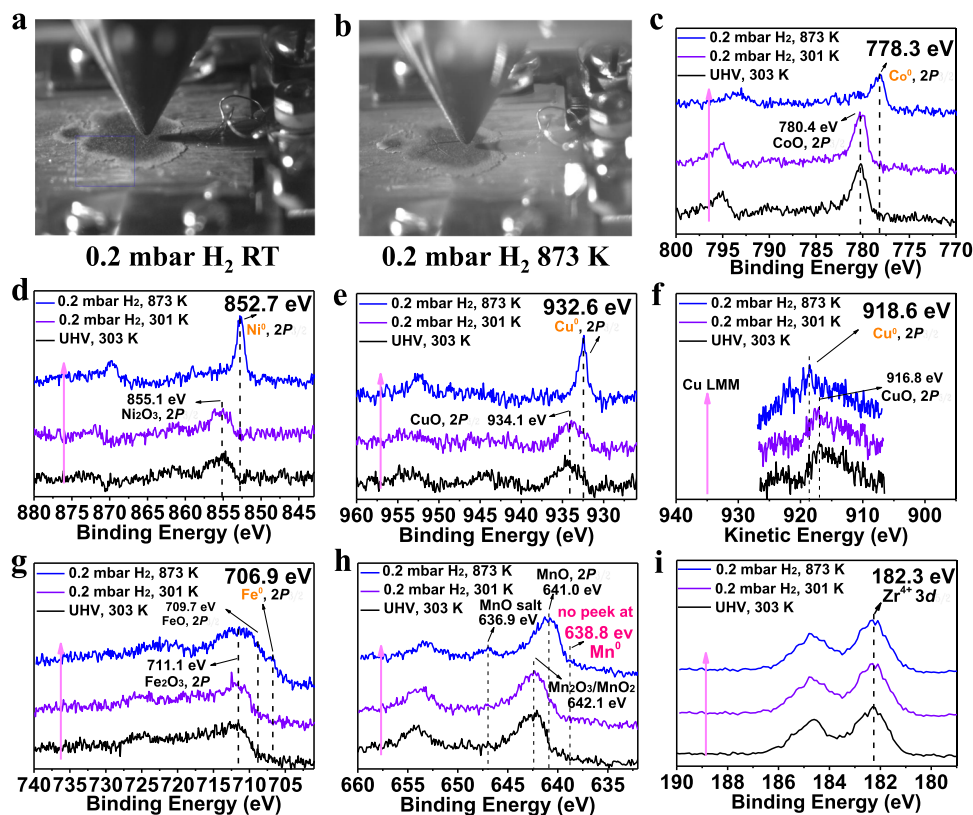


**Fig. 7** In situ XPS measurements of  $\text{Zr}_{0.5}(\text{NiFeCuMnCo})_{0.5}\text{O}_x$ . The sample was treated with X-ray exposure under UHV (traditionally ultrahigh vacuum) conditions (0.2 mbar  $\text{H}_2$ ). **a** Photograph of  $\text{Zr}_{0.5}(\text{NiFeCuMnCo})_{0.5}\text{O}_x$  under NAPXPS test at room temperature. **b** Photograph of  $\text{Zr}_{0.5}(\text{NiFeCuMnCo})_{0.5}\text{O}_x$  under NAPXPS test at 873 K. **c** Co 2p region. **d** Ni 2p region. **e**, **f** Cu 2p region. **g** Fe 2p region. **h** Mn 2p region. **i** Zr 3d region.

To figure out the self-regeneration possibility of high entropy  $\text{Zr}_{0.5}(\text{NiFeCuMnCo})_{0.5}\text{O}_x$ , the dissolution process was subsequently explored. The reduced  $\text{Zr}_{0.5}(\text{NiFeCuMnCo})_{0.5}\text{O}_x$  (treated at 600 °C,  $\text{H}_2$ ) was further exposed to oxidative environment (550 °C, air). After this cycle, the obvious XRD peaks for CoFeCuNi alloy phase disappeared (Fig. 5c). The interesting exsolution-reintegration behavior of the high entropy  $\text{ZrO}_2$  material was further proved by three redox cycles (Fig. 5c). The oxidized sample after three cycles was observed by STEM images. The elemental mapping images in different scale bars, such as 50 nm, 200 nm, 50  $\mu\text{m}$ , have been taken. As shown in Fig. 8 and Supplementary Fig. 9, all five heterometal species were evenly distributed in  $\text{ZrO}_2$  matrix, which was the same as the pristine  $\text{Zr}_{0.5}(\text{NiFeCuMnCo})_{0.5}\text{O}_x$  (Fig. 4). As expected, the entropy-added motivation may drive the reintegration of CoFeCuNi alloy NPs into the parent  $\text{ZrO}_2$  matrix in air, which contributed to the reversible self-regenerative process. All those results above suggested the feasibility of the high entropy  $\text{ZrO}_2$  as a host matrix for self-regenerative process.

**The catalytic performance of high entropy  $\text{ZrO}_2$  catalyst.** Then, the activity and thermal stability of high entropy  $\text{Zr}_{0.5}(\text{NiFeCuMnCo})_{0.5}\text{O}_x$  were explored in high temperature catalysis (Fig. 9).  $\text{CO}_2$  hydrogenation (reverse water gas shift, RWGS), with an enthalpy  $\Delta H$  of 41.3 kJ mol<sup>-1</sup>, is a typical endothermic reaction<sup>66</sup>. From the sight of both kinetics and thermodynamic, high temperature is more conducive to accelerating the reaction rate and moving the equilibrium in the direction of CO generation<sup>67</sup>. In other words, RWGS reaction is usually performed at high temperatures (e.g., 300–500 °C), whose catalysts are easy to be sintered<sup>68</sup>. In addition, a redox reaction mechanism of active sites was proposed to explain this process<sup>69</sup>. Therefore,

RWGS reaction was applied as a model process to evaluate the high entropy  $\text{ZrO}_2$  catalyst.

Compared with binary and ternary doped  $\text{ZrO}_2$  catalysts ( $\text{Zr}_{0.5}\text{Cu}_{0.5}\text{O}_x$ ,  $\text{Zr}_{0.5}\text{Mn}_{0.5}\text{O}_x$ ,  $\text{Zr}_{0.5}\text{Co}_{0.5}\text{O}_x$ ,  $\text{Zr}_{0.5}\text{Ni}_{0.5}\text{O}_x$ ,  $\text{Zr}_{0.5}\text{Fe}_{0.5}\text{O}_x$ ,  $\text{Zr}_{0.5}(\text{CuMn})_{0.5}\text{O}_x$ ) (Supplementary Fig. 10a–d), the  $\text{Zr}_{0.5}(\text{NiFeCuMnCo})_{0.5}\text{O}_x$  afforded better catalytic activity during  $\text{CO}_2$  hydrogenation (300–400 °C). When the temperature reached 400 °C, the  $\text{CO}_2$  conversion was ~29% by  $\text{Zr}_{0.5}(\text{NiFeCuMnCo})_{0.5}\text{O}_x$  and the selectivity for CO is over 90% (Fig. 9a, Supplementary Fig. 10e). Then, the long-term stability of  $\text{Zr}_{0.5}(\text{NiFeCuMnCo})_{0.5}\text{O}_x$  during  $\text{CO}_2$  hydrogenation reaction was studied. No obvious loss of catalytic activity and selectivity was found during continuous  $\text{CO}_2$  hydrogenation for 500 h (Fig. 9b). In sharp contrast, severe deactivation by the ternary doped  $\text{Zr}_{0.5}(\text{MnCu})_{0.5}\text{O}_x$  catalyst was observed in relatively short reaction time (40 h) (Fig. 9b). Meanwhile, the XRD pattern of spent  $\text{Zr}_{0.5}(\text{NiFeCuMnCo})_{0.5}\text{O}_x$  catalyst showed little tendency towards segregation or sintering, further illustrating the advantage of high entropy ( $\text{Zr}_{0.5}(\text{NiFeCuMnCo})_{0.5}\text{O}_x$ ) as the host structure (Fig. 9c). In addition, the dissolution of metal alloys somewhat underwent during  $\text{CO}_2$  atmosphere (600 °C), as suggested by the diminished XRD peaks for metallic species (Fig. 9d). Furthermore, control experiments were carried out for comparison. First, the 5%(NiFeCuCo)/ $\text{ZrO}_x$  and 10%(NiFeCuCo)/ $\text{ZrO}_x$  were synthesized by wet-impregnation method. The long-term stability of supported NiFeCuCo catalyst during  $\text{CO}_2$  hydrogenation reaction was studied at the same condition (Supplementary Fig. 11). Unfortunately, severe deactivation was observed in relatively short reaction time (1 h and 3 h). Compared with the high entropy  $\text{Zr}_{0.5}(\text{NiFeCuMnCo})_{0.5}\text{O}_x$  material (>500 h), 5%(NiFeCuCo)/ $\text{ZrO}_x$  and 10%(NiFeCuCo)/ $\text{ZrO}_x$  exhibited poor stability. Based on those results, unique properties of the



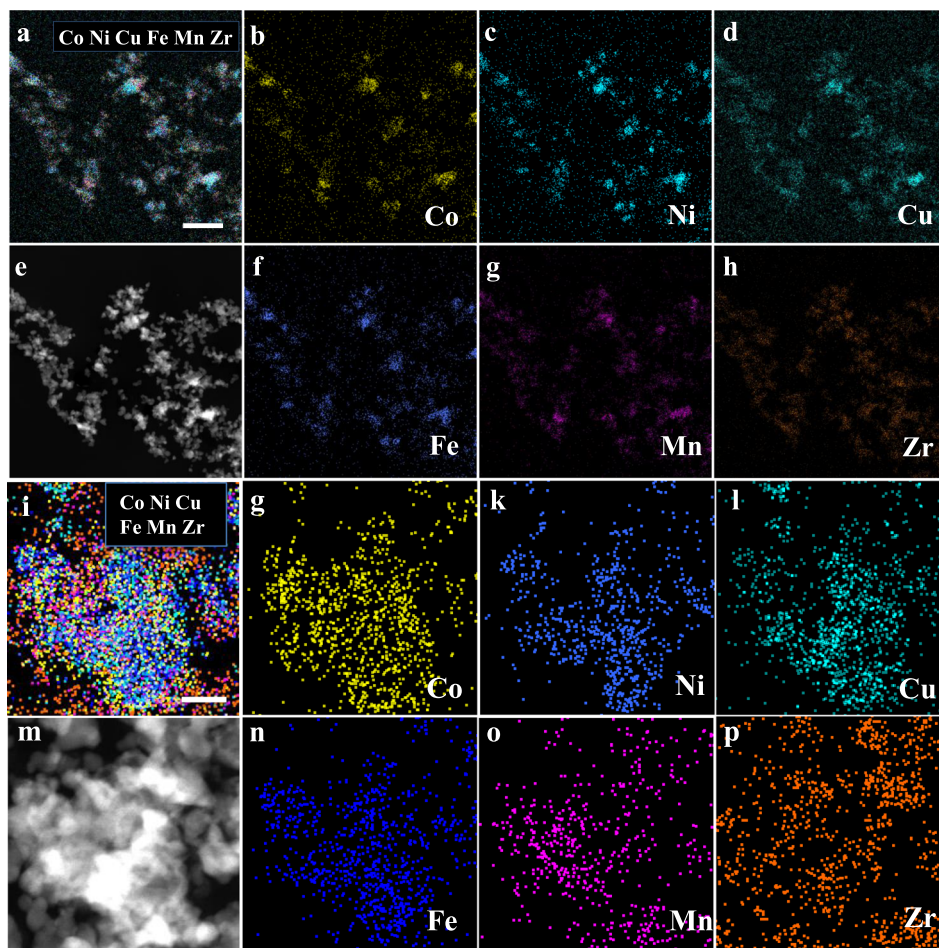


**Fig. 8** The characterization of  $\text{Zr}_{0.5}(\text{NiFeCuMnCo})_{0.5}\text{O}_x$  after three redox cycles (600 °C  $\text{H}_2$ /550 °C, Air). **a–h** STEM-HAADF image and EDS elemental maps of  $\text{Zr}_{0.5}(\text{NiFeCuMnCo})_{0.5}\text{O}_x$  after three redox cycles. Scale bar, 200 nm. **i–p** STEM-HAADF image and EDS elemental maps of  $\text{Zr}_{0.5}(\text{NiFeCuMnCo})_{0.5}\text{O}_x$  after three redox cycles. Scale bar, 50 nm.

high entropy structure indeed promoted the thermal stability of doped  $\text{ZrO}_2$  catalysts.

## Discussion

In summary, a cubic high-entropy  $\text{Zr}_{0.5}(\text{NiFeCuMnCo})_{0.5}\text{O}_x$  was designed and simply prepared. The contribution of high entropy for the sintering-resistance ability of supported transition metals was figured out, while severe particle growth occurred on  $\text{Zr}_{0.5}\text{Cu}_{0.5}\text{O}_x$  and  $\text{Zr}_{0.5}(\text{CuCoNi})_{0.5}\text{O}_x$  treated in  $\text{H}_2$ . Meanwhile, the reversible exsolution-dissolution of fine CoFeCuNi alloys on high entropy  $\text{Zr}_{0.5}(\text{NiFeCuMnCo})_{0.5}\text{O}_x$  was observed in  $\text{H}_2$ /Air treatments. Those results somewhat validate that entropy-driving force may contribute to self-regenerative process and sintering-resistance performance of supported transition metals. During high temperature catalysis (400 °C), no obvious loss of catalytic activity and little tendency towards segregation were found during continuous  $\text{CO}_2$  hydrogenation for 500 h, once again arguing for the excellent sintering-resistance ability of high entropy catalysts.

The high entropy oxide was invented in 2015<sup>29</sup> and related catalysis has been unveiled in around 2018<sup>70</sup>, and their unexpected talent for heterogeneous catalysis is a young topic<sup>63</sup>, yet full of promise. The idea of considering entropic contribution for stabilized catalyst is just the beginning, and more unique materials for heterogeneous catalysis would be inspired in the near future.

## Methods

Chemicals involved in the manuscript are used directly without purification.  $\text{ZrCl}_4$  (>99.9%, Aladdin),  $\text{NiCl}_2$  (>99%, Adamas),  $\text{FeCl}_3$  (>99%, Adamas),  $\text{CuCl}_2 \cdot 2\text{H}_2\text{O}$  (>99%, Greagent),  $\text{MnCl}_2$  (>99%, Greagent),  $\text{CoCl}_2 \cdot 6\text{H}_2\text{O}$  (>98%, Adamas),  $\text{NaOH}$  (>96%, Greagent),  $\text{NaCl}$  (>99.5%, Greagent).

The preparation of entropy-stabilized, highly doped microstructure  $\text{Zr}_{0.5}(\text{NiFeCuMnCo})_{0.5}\text{O}_x$  is as follows.  $\text{ZrCl}_4$  (2.5 mmol, 5 eq.),  $\text{NiCl}_2$  (0.5 mmol, 1 eq.),  $\text{FeCl}_3$  (0.5 mmol, 1 eq.),  $\text{CuCl}_2 \cdot 2\text{H}_2\text{O}$  (0.5 mmol, 1 eq.),  $\text{MnCl}_2$  (0.5 mmol, 1 eq.),  $\text{CoCl}_2 \cdot 6\text{H}_2\text{O}$  (0.5 mmol, 1 eq.), and  $\text{NaCl}$  (2 g) were whisked together in a 50 mL  $\text{ZrO}_2$ -milling equipment with three ball-bearings (1× diameter 1.2 cm, 2× diameter 0.8 cm). The mixtures were ball milled for 1 h. Then the  $\text{NaOH}$  (15.5 mmol) was added into the system and the mixtures were ball milled for another 1 h. Calcination of the as-synthesized powder was performed into a muffle oven in air at 400 °C, 500 °C, 550 °C, 600 °C for 3 h (2 K  $\text{min}^{-1}$  to appointed temperature) and then cooled down to room temperature. The powder was washed three times by deionized water, and then washed with ethanol. Then as-made samples ( $\text{Zr}_{0.5}(\text{NiFeCuMnCo})_{0.5}\text{O}_x$ ) were put into a vacuum drying oven and dried at 70 °C for 12 h. The synthesis of other doped  $\text{ZrO}_2$  materials for comparative experiments can be found in Supplementary Methods section. The obtained samples were referred to as  $\text{Zr}_{0.5}\text{Cu}_{0.5}\text{O}_x$ ,  $\text{Zr}_{0.5}\text{Mn}_{0.5}\text{O}_x$ ,  $\text{Zr}_{0.5}\text{Co}_{0.5}\text{O}_x$ ,  $\text{Zr}_{0.5}\text{Ni}_{0.5}\text{O}_x$ ,  $\text{Zr}_{0.5}\text{Fe}_{0.5}\text{O}_x$ ,  $\text{Zr}_{0.5}(\text{CuMn})_{0.5}\text{O}_x$ ,  $\text{Zr}_{0.5}(\text{NiFeCuMnCo})_{0.5}\text{O}_x$ .

The powder X-ray diffraction (D8 Advance, Bruker) operated at 40 kV and 40 mA and the pattern was recorded in the range of 20–80°. The material was characterized by  $\text{N}_2$  adsorption isotherms (Tristar II 3020 S1N1878) at 77 K. NAPXPS measurements were carried out on an SPECS system equipped with a differentially pumped Phoibos hemispherical electron energy analyzer using monochromatic Al K $\alpha$  radiation (1486.6 eV). The in situ characterization was performed in the 873 K 0.2 mbar  $\text{H}_2$  reduction condition. The heating rate was 5 K  $\text{min}^{-1}$  from 301 K to 873 K. HAADF-STEM (Talos F200X G2, FEI). Leica EM TXP (Mingrui GC2060, China). Inductive Coupled Plasma Emission Spectrometer (iCAP7600, made by Thermo., USA).

The as-made catalysts (75 or 50 mg) were used for the  $\text{H}_2$ -TPR experiments (Micromeritics Autochem II 2920). The material was pretreated in Ar (30 mL  $\text{min}^{-1}$ )



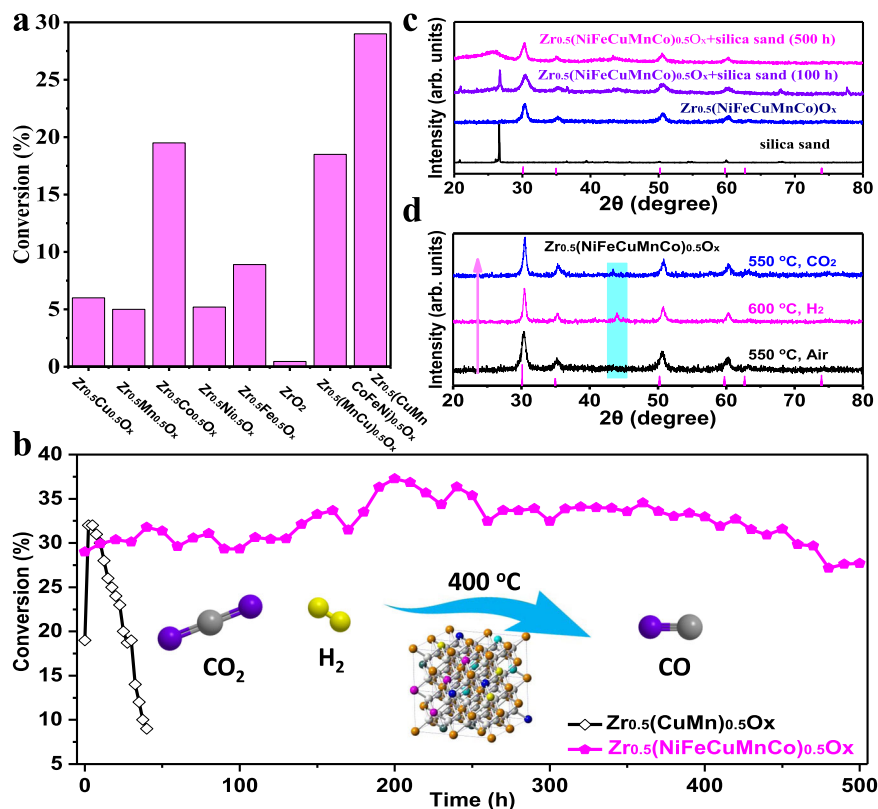


**Fig. 9** Catalytic performance of doped ZrO<sub>2</sub> catalysts. **a** catalytic performance of Zr<sub>0.5</sub>Cu<sub>0.5</sub>O<sub>x</sub>, Zr<sub>0.5</sub>Mn<sub>0.5</sub>O<sub>x</sub>, Zr<sub>0.5</sub>Co<sub>0.5</sub>O<sub>x</sub>, Zr<sub>0.5</sub>Ni<sub>0.5</sub>O<sub>x</sub>, Zr<sub>0.5</sub>Fe<sub>0.5</sub>O<sub>x</sub>, Zr<sub>0.5</sub>(CuMn)<sub>0.5</sub>O<sub>x</sub>, and Zr<sub>0.5</sub>(NiFeCuMnCo)<sub>0.5</sub>O<sub>x</sub> in CO<sub>2</sub> hydrogenation at 400 °C. **b** P-XRD patterns of reused Zr<sub>0.5</sub>(NiFeCuMnCo)<sub>0.5</sub>O<sub>x</sub> samples after 100 h and 500 h on steam. **c** The P-XRD patterns of phase evolution between H<sub>2</sub>/CO<sub>2</sub> conditions. **d** Thermal stability tests of Zr<sub>0.5</sub>(NiFeCuMnCo)<sub>0.5</sub>O<sub>x</sub> and Zr<sub>0.5</sub>(CuMn)<sub>0.5</sub>O<sub>x</sub> in CO<sub>2</sub> hydrogenation. arb. units: arbitrary unit.

at 300 °C for 60 min and then cooled to the room temperature. Then, the 5% H<sub>2</sub> in Ar (30 mL min<sup>-1</sup>) was switched on in a heating rate of 10 °C min<sup>-1</sup>. Finally, the H<sub>2</sub> consumption of the as-made materials was monitored by a TCD detector.

The RWGS reaction worked at atmospheric pressure in a fixed-bed quartz reactor. Firstly, 30 mg catalyst and 100 mg quartz sand were mixed together well. Then, the catalyst with quartz was exposed to a stream of feed gas (H<sub>2</sub>:CO<sub>2</sub> = 3:1, 10 mL min<sup>-1</sup>). When the catalyst reached the appointed temperature, the gaseous products were analyzed by gas chromatograph with a TCD and FID detector.

Detailed procedures are in the Supplementary Methods section.

## Data availability

The authors declare data supporting the findings of this study are available within the paper and its Supplementary Information. All data are available from the authors on reasonable request.

Received: 17 February 2021; Accepted: 13 September 2021;

Published online: 11 October 2021

## References

- Grant, J. T., Venegas, J. M., McDermott, W. P. & Hermans, I. Aerobic oxidations of light alkanes over solid metal oxide catalysts. *Chem. Rev.* **118**, 2769–2815 (2018).
- Zhang, Z. Q. et al. The simplest construction of single-site catalysts by the synergism of micropore trapping and nitrogen anchoring. *Nat. Commun.* **10**, 7 (2019).
- van der Lee, M. K., van Dillen, J., Bitter, J. H. & de Jong, K. P. Deposition precipitation for the preparation of carbon nanofiber supported nickel catalysts. *J. Am. Chem. Soc.* **127**, 13573–13582 (2005).
- Kondrat, S. A. et al. Stable amorphous georgeite as a precursor to a high-activity catalyst. *Nature* **531**, 83–87 (2016).
- Xu, S. et al. Extending the limits of Pt/C catalysts with passivation-gas-incorporated atomic layer deposition. *Nat. Catal.* **1**, 624–630 (2018).
- Weidenhof, B. et al. High-throughput screening of nanoparticle catalysts made by flame spray pyrolysis as hydrocarbon/NO oxidation catalysts. *J. Am. Chem. Soc.* **131**, 9207–9219 (2009).
- Corma, A. Heterogeneous catalysis: understanding for designing, and designing for applications. *Angew. Chem. Int. Ed.* **55**, 6112–6113 (2016).
- Cargnello, M. et al. Control of metal nanocrystal size reveals metal-support interface role for ceria catalysts. *Science* **341**, 771–773 (2013).
- Kattel, S., Ramirez, P. J., Chen, J. G., Rodriguez, J. A. & Liu, P. Active sites for CO<sub>2</sub> hydrogenation to methanol on Cu/ZnO catalysts. *Science* **355**, 1296–1299 (2017).
- Corral-Pérez, J. J. et al. Decisive role of perimeter sites in silica-supported Ag nanoparticles in selective hydrogenation of CO<sub>2</sub> to methyl formate in the presence of methanol. *J. Am. Chem. Soc.* **140**, 13884–13891 (2018).
- Abdel-Mageed, A. M. et al. Negative charging of Au nanoparticles during methanol synthesis from CO<sub>2</sub>/H<sub>2</sub> on a Au/ZnO catalyst: insights from operando IR and near-ambient-pressure XPS and XAS measurements. *Angew. Chem. Int. Ed.* **58**, 10325–10329 (2019).
- Zhou, Z.-Y., Tian, N., Li, J.-T., Broadwell, I. & Sun, S.-G. Nanomaterials of high surface energy with exceptional properties in catalysis and energy storage. *Chem. Soc. Rev.* **40**, 4167–4185 (2011).
- Wang, L., Wang, L., Meng, X. & Xiao, F.-S. New strategies for the preparation of sinter-resistant metal-nanoparticle-based catalysts. *Adv. Mater.* **31**, 1901905 (2019).
- Yan, W., Mahurin, S. M., Pan, Z., Overbury, S. H. & Dai, S. Ultrastable Au nanocatalyst supported on surface-modified TiO<sub>2</sub> nanocrystals. *J. Am. Chem. Soc.* **127**, 10480–10481 (2005).
- Wang, Y. et al. Avoiding self-poisoning: a key feature for the high activity of Au/Mg(OH)<sub>2</sub> catalysts in continuous low-temperature CO oxidation. *Angew. Chem. Int. Ed.* **56**, 9597–9602 (2017).
- Nishihata, Y. et al. Self-regeneration of a Pd-perovskite catalyst for automotive emissions control. *Nature* **418**, 164–167 (2002).
- Katz, M. B. et al. Self-regeneration of Pd-LaFeO<sub>3</sub> catalysts: new insight from atomic-resolution electron microscopy. *J. Am. Chem. Soc.* **133**, 18090–18093 (2011).

18. Neagu, D., Tsekouras, G., Miller, D. N., Menard, H. & Irvine, J. T. In situ growth of nanoparticles through control of non-stoichiometry. *Nat. Chem.* **5**, 916–923 (2013).
19. Lv, H. et al. Atomic-scale insight into exsolution of CoFe alloy nanoparticles in La<sub>0.4</sub>Sr<sub>0.6</sub>Co<sub>0.2</sub>Fe<sub>0.7</sub>Mo<sub>0.1</sub>O<sub>3-δ</sub> with efficient CO<sub>2</sub> electrolysis. *Angew. Chem. Int. Ed.* **59**, 15968–15973 (2020). 358.
20. Tanaka, H. et al. Self-regenerating Rh- and Pt-based perovskite catalysts for automotive-emissions control. *Angew. Chem. Int. Ed.* **45**, 5998–6002 (2006).
21. Lv, H. et al. In situ investigation of reversible exsolution/dissolution of CoFe alloy nanoparticles in a Co-Doped Sr<sub>2</sub>Fe<sub>1.5</sub>Mo<sub>0.5</sub>O<sub>6-δ</sub> cathode for CO<sub>2</sub> electrolysis. *Adv. Mater.* **32**, 1906193 (2020).
22. Zhang, S. et al. New atomic-scale insight into self-regeneration of Pt-CaTiO<sub>3</sub> catalysts: incipient redox-induced structures revealed by a small-angle tilting STEM technique. *J. Phys. Chem. C.* **121**, 17348–17353 (2017).
23. Neagu, D. et al. Nano-socketed nickel particles with enhanced coking resistance grown in situ by redox exsolution. *Nat. Commun.* **6**, 8120 (2015).
24. Lv, H. et al. In situ investigation of reversible exsolution/dissolution of CoFe alloy nanoparticles in a Co-Doped Sr<sub>2</sub>Fe<sub>1.5</sub>Mo<sub>0.5</sub>O<sub>6-δ</sub> cathode for CO<sub>2</sub> electrolysis. *Adv. Mater.* **32**, 1906193 (2020).
25. Bian, L. et al. Electrochemical performance and stability of La<sub>0.5</sub>Sr<sub>0.5</sub>Fe<sub>0.9</sub>Nb<sub>0.1</sub>O<sub>3-δ</sub> symmetric electrode for solid oxide fuel cells. *J. Power Sources* **399**, 398–405 (2018).
26. Yu, X., Long, W., Jin, F. & He, T. Cobalt-free perovskite cathode materials SrFe<sub>1-x</sub>Ti<sub>x</sub>O<sub>3-δ</sub> and performance optimization for intermediate-temperature solid oxide fuel cells. *Electrochim. Acta* **123**, 426–434 (2014).
27. Yang, Z. et al. La<sub>0.7</sub>Sr<sub>0.3</sub>Fe<sub>0.7</sub>Ga<sub>0.3</sub>O<sub>3-δ</sub> as electrode material for a symmetrical solid oxide fuel cell. *RSC Adv.* **5**, 2702–2705 (2015).
28. Miracle, D. B. & Senkov, O. N. A critical review of high entropy alloys and related concepts. *Acta Mater.* **122**, 448–511 (2017).
29. Rost, C. M. et al. Entropy-stabilized oxides. *Nat. Commun.* **6**, 8485 (2015).
30. Sarkar, A. et al. High entropy oxides for reversible energy storage. *Nat. Commun.* **9**, 3400 (2018).
31. Zhang, R.-Z., Gucci, F., Zhu, H., Chen, K. & Reece, M. J. Data-driven design of ecofriendly thermoelectric high-entropy sulfides. *Inorg. Chem.* **57**, 13027–13033 (2018).
32. Zhao, X., Xue, Z., Chen, W., Wang, Y. & Mu, T. Eutectic synthesis of high-entropy metal phosphides for electrocatalytic water splitting. *ChemSusChem* **13**, 2038–2042 (2020).
33. Jin, T. et al. Mechanochemical-assisted synthesis of high-entropy metal nitride via a soft urea strategy. *Adv. Mater.* **30**, 1707512 (2018).
34. Sure, J., Sri Maha Vishnu, D., Kim, H.-K. & Schwandt, C. Facile electrochemical synthesis of nanoscale (TiNbTaZrHf)C high-entropy carbide powder. *Angew. Chem. Int. Ed.* **59**, 11830–11835 (2020).
35. Gild, J. et al. High-entropy metal diborides: a new class of high-entropy materials and a new type of ultrahigh temperature ceramics. *Sci. Rep.* **6**, 37946 (2016).
36. Chen, H. et al. An ultrastable heterostructured oxide catalyst based on high-entropy materials: a new strategy toward catalyst stabilization via synergistic interfacial interaction. *Appl. Catal. B Environ.* **276**, 119155 (2020).
37. Singh, P. et al. Design of high-strength refractory complex solid-solution alloys. *NPJ Comput. Mater.* **4**, 16 (2018).
38. Otroshchenko, T. et al. ZrO<sub>2</sub>-based alternatives to conventional propane dehydrogenation catalysts: active sites, design, and performance. *Angew. Chem. Int. Ed.* **54**, 15880–15883 (2015).
39. García-Moncada, N. et al. A direct in situ observation of water-enhanced proton conductivity of Eu-doped ZrO<sub>2</sub>: Effect on WGS reaction. *Appl. Catal. B Environ.* **231**, 343–356 (2018).
40. Manzoor, A., Pandey, S., Chakraborty, D., Phillpot, S. R. & Aidhy, D. S. Entropy contributions to phase stability in binary random solid solutions. *NPJ Comput. Mater.* **4**, 47 (2018).
41. Dawson, J. A. & Tanaka, I. Proton incorporation and trapping in ZrO<sub>2</sub> grain boundaries. *J. Mater. Chem. A* **2**, 1400–1408 (2014).
42. Montini, T., Melchionna, M., Monai, M. & Fornasiero, P. Fundamentals and catalytic applications of CeO<sub>2</sub>-based materials. *Chem. Rev.* **116**, 5987–6041 (2016).
43. Chen, H. et al. Entropy-stabilized metal oxide solid solutions as CO oxidation catalysts with high-temperature stability. *J. Mater. Chem. A* **6**, 11129–11133 (2018).
44. Chen, H. et al. A new spinel high-entropy oxide (Mg<sub>0.2</sub>Ti<sub>0.2</sub>Zn<sub>0.2</sub>Cu<sub>0.2</sub>Fe<sub>0.2</sub>)<sub>3</sub>O<sub>4</sub> with fast reaction kinetics and excellent stability as an anode material for lithium ion batteries. *RSC Adv.* **10**, 9736–9744 (2020).
45. Feng, D. et al. Holey lamellar high-entropy oxide as an ultra-high-activity heterogeneous catalyst for solvent-free aerobic oxidation of benzyl alcohol. *Angew. Chem. Int. Ed.* **59**, 19503–19509 (2020).
46. Zhan, W. et al. Incorporating rich mesoporosity into a ceria-based catalyst via mechanochemistry. *Chem. Mater.* **29**, 7323–7329 (2017).
47. Li, H.-F., Zhang, N., Chen, P., Luo, M.-F. & Lu, J.-Q. High surface area Au/CeO<sub>2</sub> catalysts for low temperature formaldehyde oxidation. *Appl. Catal. B Environ.* **110**, 279–285 (2011).
48. Khalakhan, I. et al. Irreversible structural dynamics on the surface of bimetallic PtNi alloy catalyst under alternating oxidizing and reducing environments. *Appl. Catal. B Environ.* **264**, 118476 (2020).
49. Kwon, O. et al. Exsolution trends and co-segregation aspects of self-grown catalyst nanoparticles in perovskites. *Nat. Commun.* **8**, 15967 (2017).
50. Yu, K., Lou, L.-L., Liu, S. & Zhou, W. Asymmetric oxygen vacancies: the intrinsic redox active sites in metal oxide catalysts. *Adv. Sci.* **7**, 1901970 (2020).
51. Ruiz Puiggollers, A., Schlexer, P., Tosoni, S. & Pacchioni, G. Increasing oxide reducibility: the role of metal/oxide interfaces in the formation of oxygen vacancies. *ACS Catal.* **7**, 6493–6513 (2017).
52. Hengne, A. M. & Rode, C. V. Cu-ZrO<sub>2</sub> nanocomposite catalyst for selective hydrogenation of levulinic acid and its ester to  $\gamma$ -valerolactone. *Green. Chem.* **14**, 1064–1072 (2012).
53. Zhao, B. et al. Comparative study of Mn/TiO<sub>2</sub> and Mn/ZrO<sub>2</sub> catalysts for NO oxidation. *Catal. Commun.* **56**, 36–40 (2014).
54. Jeon, W., Choi, I.-H., Park, J.-Y., Lee, J.-S. & Hwang, K.-R. Alkaline wet oxidation of lignin over Cu-Mn mixed oxide catalysts for production of vanillin. *Catal. Today* **352**, 95–103 (2020).
55. Zhang, L., Lin, J. & Chen, Y. Studies of surface NiO species in NiO/SiO<sub>2</sub> catalysts using temperature-programmed reduction and X-ray diffraction. *J. Chem. Soc. Faraday Trans.* **88**, 2075–2078 (1992).
56. Li, A. et al. Synthesis of dimethyl carbonate from methanol and CO<sub>2</sub> over Fe-Zr mixed oxides. *J. CO<sub>2</sub> Util.* **19**, 33–39 (2017).
57. Song, H., Zhang, L. & Ozkan, U. S. Effect of synthesis parameters on the catalytic activity of Co-ZrO<sub>2</sub> for bio-ethanol steam reforming. *Green. Chem.* **9**, 686–694 (2007).
58. Johnson, G. R. & Bell, A. T. Role of ZrO<sub>2</sub> in promoting the activity and selectivity of Co-based Fischer-Tropsch synthesis catalysts. *ACS Catal.* **6**, 100–114 (2016).
59. Zhang, P. et al. Mesoporous MnCeOx solid solutions for low temperature and selective oxidation of hydrocarbons. *Nat. Commun.* **6**, 8446 (2015).
60. Song, C. et al. Size dependence of structural parameters in fcc and hcp Ru nanoparticles, revealed by Rietveld refinement analysis of high-energy X-ray diffraction data. *Sci. Rep.* **6**, 31400 (2016).
61. Powell, C. J. Recommended Auger parameters for 42 elemental solids. *Spectrosc. Relat. Phenom.* **185**, 1–3 (2012).
62. Kundu, A. K. & Menon, K. S. R. Growth and characterization of ultrathin epitaxial MnO film on Ag(001). *J. Cryst. Growth* **446**, 85–91 (2016).
63. Li, T. et al. Denary oxide nanoparticles as highly stable catalysts for methane combustion. *Nat. Catal.* **4**, 62–70 (2021).
64. Cantor, B., Chang, I. T. H., Knight, P. & Vincent, A. J. B. Microstructural development in equiatomic multicomponent alloys. *Mater. Sci. Eng. A* **375–377**, 213–218 (2004).
65. Gludovatz, B. et al. A fracture-resistant high-entropy alloy for cryogenic applications. *Science* **345**, 1153 (2014).
66. Riedel, T., Schaub, G., Jun, K.-W. & Lee, K.-W. Kinetics of CO<sub>2</sub> hydrogenation on a K-promoted Fe catalyst. *Ind. Eng. Chem. Res.* **40**, 1355–1363 (2001).
67. Li, Y. F. et al. Cu atoms on nanowire Pd/HyWO<sub>3-x</sub> bronzes enhance the solar reverse water gas shift reaction. *J. Am. Chem. Soc.* **141**, 14991–14996 (2019).
68. Nelson, N. C., Chen, L., Meira, D., Kovarik, L. & Szanyi, J. In situ dispersion of palladium on TiO<sub>2</sub> during reverse water-gas shift reaction: formation of atomically dispersed palladium. *Angew. Chem. Int. Ed.* **59**, 17657–17663 (2020).
69. Daza, Y. A., Kent, R. A., Yung, M. M. & Kuhn, J. N. Carbon dioxide conversion by reverse water-gas shift chemical looping on perovskite-type oxides. *Ind. Eng. Chem. Res.* **53**, 5828–5837 (2014).
70. Oses, C., Toher, C. & Curtarolo, S. High-entropy ceramics. *Nat. Rev. Mater.* **5**, 295–309 (2020).

## Acknowledgements

This work was supported by the National Key R&D Program of China (2020YFB0606401), National Natural Science Foundation of China (Grant No. 21776174), Shanghai Rising Star Program (20QA1405200), and Inner Mongolia Erdos Group. S.D. was supported by the U.S. Department of Energy, Office of Science, Office of Basic Energy Sciences, Chemical Sciences, Geosciences, and Biosciences Division, Catalysis Science program.

## Author contributions

P.F.Z. designed the experiments. S.T.H. and X.F.M. together completed those experiments. P.F.Z. and S.T.H. wrote the paper. S.D., Y.S. and J.F.B. discussed the results and commented on the manuscript. M.S.C. and Q.Y.Z. helped with the in situ XPS measurements.

**Competing interests**

The authors declare no competing interests.

**Additional information**

**Supplementary information** The online version contains supplementary material available at <https://doi.org/10.1038/s41467-021-26160-8>.

**Correspondence** and requests for materials should be addressed to Pengfei Zhang.

**Peer review information** *Nature Communications* thanks Ben Breitung and the other, anonymous, reviewers for their contribution to the peer review of this work.

**Reprints and permission information** is available at <http://www.nature.com/reprints>

**Publisher's note** Springer Nature remains neutral with regard to jurisdictional claims in published maps and institutional affiliations.



**Open Access** This article is licensed under a Creative Commons Attribution 4.0 International License, which permits use, sharing, adaptation, distribution and reproduction in any medium or format, as long as you give appropriate credit to the original author(s) and the source, provide a link to the Creative Commons license, and indicate if changes were made. The images or other third party material in this article are included in the article's Creative Commons license, unless indicated otherwise in a credit line to the material. If material is not included in the article's Creative Commons license and your intended use is not permitted by statutory regulation or exceeds the permitted use, you will need to obtain permission directly from the copyright holder. To view a copy of this license, visit <http://creativecommons.org/licenses/by/4.0/>.

© The Author(s) 2021